



Top illuminated organic photodetectors with dielectric/metal/dielectric transparent anode



Hyunsoo Kim, Kyu-Tae Lee, Chumin Zhao, L. Jay Guo, Jerzy Kanicki*

Department of Electrical Engineering and Computer Science, University of Michigan, Ann Arbor, MI 48109, USA

ARTICLE INFO

Article history:

Received 4 December 2014

Received in revised form 8 February 2015

Accepted 8 February 2015

Available online 14 February 2015

Keywords:

Organic electronics

Photodetectors

MoO₃/Ag/MoO₃

Top-illumination

Inverted structure

ABSTRACT

The top illuminated organic photodetectors (OPDs) with a Dielectric/Metal/Dielectric (DMD) transparent anode are fabricated. The transparent electrode is composed of molybdenum trioxide (MoO₃)/silver (Ag)/MoO₃ layers and zinc oxide (ZnO)/aluminum (Al) is used for bottom cathode. The optimized DMD electrode has an optical transmittance of 85.7% at the wavelength of 546 nm and sheet resistance of ~6 Ω/sq. The fabricated OPDs exhibit a high detectivity and wide range linearity.

© 2015 Elsevier B.V. All rights reserved.

1. Introduction

Over two decades, organic photovoltaics and photodetectors have been extensively studied due to their easy deposition methods, large-area processing capabilities, and fine tunability of optical absorption coefficients [1,2]. Especially, organic photodiodes (OPD) have been actively studied as potential low-cost, high-performance alternatives to amorphous silicon (a-Si) photodiode for flat panel imagers [3–5]. Among various kinds of the imagers, indirect type imager based on CsI(Tl) scintillator looks very promising for OPD application due to its reduced lateral light scattering, high light output, fast response time, and suitable peak emission spectra [6,7]. Among various organic materials for such application, Poly(3-hexylthiophene-2,5-diyl):Phenyl-C₆₁-butyric acid methyl ester (P3HT:PCBM) bulk heterojunction (BHJ) blend system appears to be very desirable candidate [4,5,7–9]. Ng et al. used 4 μm thick poly[(2-methoxy-5-ethylhexyloxy)-1,4-phenylenevinylene] (MEHPPV):PCBM BHJ blend layer as photoactive

layer in combination with a flexible a-Si thin-film transistor (TFT) backplane to realize an imager array with 35% external quantum efficiency [3]. They used solution processed ITO nanoparticles as top transparent electrode which had a very high sheet resistance of 1 MΩ/sq, resulting in significant current loss during signal readout. Alternatively, Tedde et al. demonstrated a concept of a-Si:H TFTs active pixel sensor (APS) imager integrated with the OPD. The APS provides on-pixel amplification up to 10 compared to passive pixel sensor (PPS) [4]. They adapted conventional structure of OPDs with top Ca/Al transparent cathode. When low-workfunction metals are used as transparent electrode, post-process encapsulation is required. The long-term stability of such devices cannot be guaranteed, also the Ca/Al transparency is rather low. To enhance the device stability in air, the inverted organic solar cell or photodiode architectures are investigated. In such devices a high workfunction metal such as Au, Ag, or PEDOT:PSS are used as top transparent electrodes [10–16]. Although a large number of works have been reported for inverted type organic solar cells [10–14] or inverted type organic photodetector with the bottom illumination [15], only a few inverted type organic photodetectors with top

* Corresponding author.

E-mail address: kanicki@umich.edu (J. Kanicki).

illumination geometry have been reported so far. For example, Baierl et al. demonstrated the inverted type P3HT:PCBM OPD with PEDOT:PSS as a top electrode [17,18]. In such device configuration the PEDOT:PSS suffers from a high acidity, hygroscopic behavior, resulting in inferior stability [19]. Alternatively, ultra-thin metallic films can also be used as a transparent electrode in OPV and OPD application [4,5,20,21]. In such configuration, the reflection from the metal surface is too high and a large portion of incident light can be wasted. To suppress such high reflections, an optically transparent dielectric material can be employed as an anti-reflection layer, leading to the Dielectric/Metal/Dielectric (DMD) multilayer electrode configuration. Although a number of papers on the application of the DMD transparent electrode to organic light emitting diode and organic solar cell have been published [22–26], to our best knowledge, no research on the top anode, top-illumination OPD with the DMD configuration has been reported. In this paper, we demonstrate a top-anode, top-illumination OPD with engineered MoO₃/Ag/MoO₃ DMD semi-transparent electrode that could be used for large-area imager application. The optical simulation and experimental measurement are conducted to investigate the effect of the DMD semi-transparent electrode on the OPD properties. Also, OPD electrical characteristics including current–voltage properties, quantum efficiency, noise equivalent power, and detectivity are evaluated.

2. Experimental

2.1. Device fabrication

Low-cost soda lime glass substrates (Asahi glass) were cleaned by acetone, isopropyl alcohol, and deionized water by sonication for 5 min for each process, and treated by oxygen plasma for 5 min subsequently. 100 nm of aluminum layer was thermally evaporated using shadow mask for patterning bottom cathode. ZnO sol–gel solution was prepared by dissolving 0.5 M of zinc acetate dihydrate (Zn(CH₃COO)₂·2H₂O, Sigma Aldrich) as a precursor in 2-methoxyethanol (2ME, Sigma Aldrich) solvent. 0.5 M of mono-ethanolamine was added as a stabilizer and the mixture was vigorously stirred at a temperature of 60 °C for 4 h. The solution was then cooled down and aged for more than 24 h. The synthesized ZnO solution was spin-coated on top of the patterned cathode layer with spin-coating speed of 2000 rpm for 30 s and annealed at 150 °C for 20 min, yielding 40 nm thickness of ZnO layer. The substrates were transferred into a glove box with nitrogen atmosphere for deposition of photoactive layer. 25 mg of P3HT (Rieke Metals) and 25 mg of PCBM (American Dye Source, Purity: >99.5%) were mixed into 1 mL of dichlorobenzene (DCB) and stirred by magnetic bar overnight for the BHJ solution. The solution was filtered by 0.45 μm syringe filter and then spin-coated onto the ZnO layer with different spin-coating speed to realize OPDs with active layer thickness of 200 nm, 320 nm and 450 nm. To prevent complete drying of P3HT:PCBM film, the spin-coating timing was adjusted for each process. The active layers were then solvent-assisted annealed [27] for

30 min to 1 h to ensure fully dried films in N₂ atmosphere. The substrates were transferred into thermal evaporator for deposition of 5 nm MoO₃, 10 nm silver and 35 nm MoO₃ subsequently. A shadow mask was used for top anode fabrication. All the devices were encapsulated with a thin slide glass sealed by UV curable epoxy resin. The device size was 0.04 cm² with square shape.

2.2. Device measurement

Optical transmittance and absorbance spectra of the semitransparent DMD, DM multilayer, and P3HT:PCBM BHJ film were measured using Agilent CARY-5E UV–vis spectrometer. Optical reflectance of the DMD, DM electrode were measured by Filmetrics F20 thin-film measurement system. Sheet resistances of the electrodes are measured by 4-point probe method. A solar simulator (Oriel) equipped with Xenon lamp and band pass filter with peak wavelength 546 nm (FWHM = 2 nm), was used for the current density–voltage (*J*–*V*) characteristic measurement under illumination. The irradiance of the illuminated light was measured by Newport power meter. The *J*–*V* characteristics of all the organic photodiode under illumination and dark conditions were measured by HP2416A semiconductor measurement system with a probe station in a dark Faraday cage. External Quantum Efficiency (EQE) was measured with a setting of lock-in amplifier (Stanford Research Systems SRS 830), monochromator with a 100 W halogen tungsten lamp, light chopper, and UV-enhanced silicon photodetector (Newport UV808) for calibration.

2.3. Methods

Optical modeling method and detailed description of the OPD figures of merits can be found in the [Supplementary Materials](#).

3. Results and discussion

3.1. DMD top electrode simulation, characterization, and optimization

The Dielectric/Metal/Dielectric (DMD) electrode in comparison to other transparent top electrode has desirable properties such as (i) the DMD electrode has anti-reflective MoO₃ dielectric layer on top, which maximizes the transmission of the light of interest, and (ii) the passivation of the top electrode with the additional MoO₃ layer allows direct deposition (e.g. thermal evaporation [28]) of CsI(Tl) scintillator materials, which is beneficial in achieving a higher scintillator gain [7]. Fig. 1 shows the schematic of the fabricated top illuminated OPD. To find optimum layer thicknesses ensuring that a maximum amount of incident light can pass through the top DMD multilayer transparent electrode, an optical simulation is carried out based on refractive indices of all the OPD layers measured by a spectroscopic ellipsometer. The measured refractive indices of MoO₃ and Ag layers over wavelength from 400 nm to 800 nm are shown in Fig. S1 (Supplementary

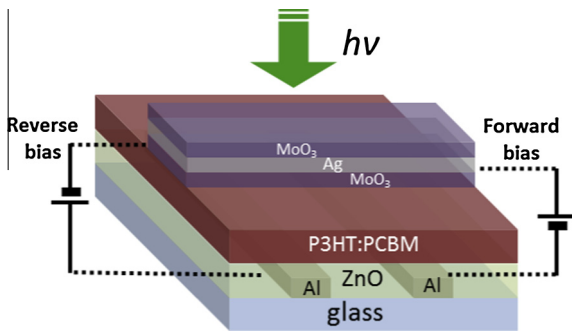


Fig. 1. Device structure of the top anode OPD with top illumination.

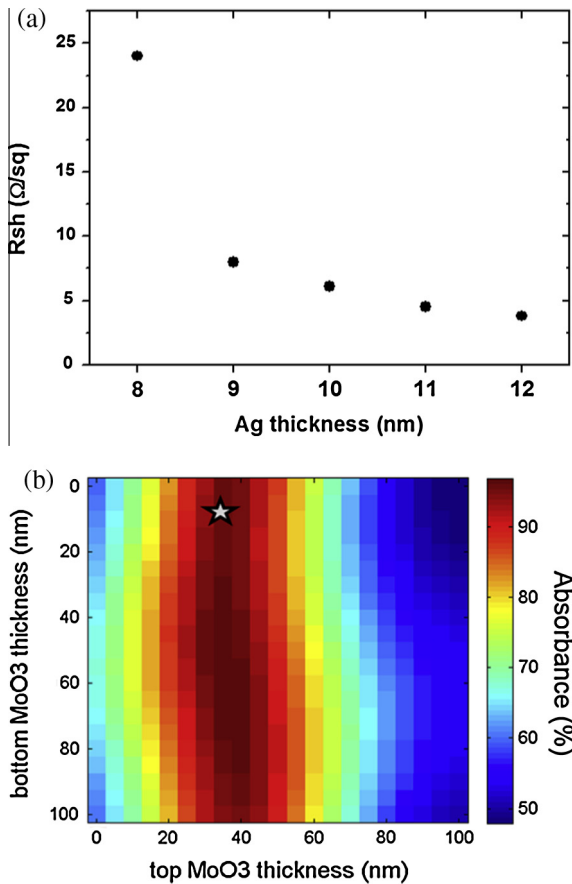


Fig. 2. (a) Sheet resistance of the MoO₃ 5 nm/Ag varied/MoO₃ 35 nm structure fabricated on glass as a function of the thickness of the Ag interlayer. (b) Simulated 2D absorption spectrum with different bottom and top MoO₃ thickness in DMD structure with fixed Ag layer thickness of 10 nm. The color bar represents the absorption in P3HT:PCBM at 546 nm. (For interpretation of the references to color in this figure legend, the reader is referred to the web version of this article.)

Materials). The index values of all the layers in the OPD at the wavelength of 546 nm are summarized in Table S1. Prior to determining the optimum thickness of each layer of the DMD electrode, we need to fix the Ag interlayer thickness which ensures both a low sheet resistance and a high optical transmittance. Fig. 2a shows the variation

of the sheet resistance of the DMD structure with MoO₃ 5 nm/Ag varied/MoO₃ 35 nm on glass as a function of the thickness of the Ag interlayer. As shown in the figure, silver thickness higher than 9 nm gives sheet resistance under 10 Ω/sq which is suitable for a large area imager. High sheet resistance of 24 Ω/sq of the DMD layer with 8 nm Ag thickness shown in the figure can be attributed to the discontinuous film morphology with aggregated Ag islands formation [29]. Meanwhile, the significant decrease of the R_{sh} for Ag thickness above 9 nm assures the formation of the continuous metal film. We fixed Ag thickness to 10 nm for the DMD multilayer; the sheet resistance of the DMD film was 6.2 Ω/sq , which is much lower than 10 Ω/sq of standard ITO. Next, to find the optimum thickness of the bottom and top MoO₃ dielectric layer for light transmission, the transfer matrix method approach was applied to the whole OPD structure with varying top and bottom MoO₃ thickness. Fig. 2b shows a simulated contour plot of the light absorption in the P3HT:PCBM active layer of the OPD structure as functions of top and bottom MoO₃ thickness. Fixed thickness of Al = 100 nm, ZnO = 40 nm, P3HT:PCBM = 320 nm, and Ag = 10 nm are used. In this simulation, a monochromatic light at the wavelength 546 nm is chosen since it corresponds to an emission peak of the CsI(Tl) scintillator [7]. As can be seen from the figure, the highest absorption in the active layer can be achieved when the top MoO₃ layer thickness is around 35 nm, indicating light absorbance over 90% by P3HT:PCBM film. Since the bottom MoO₃ layer not only transmits the incident light but also transports the photogenerated charges [23,29], it is required to optimize this thickness for both light transmission and carrier transport. From the simulation data we can conclude that the maximum absorption is attained with a combination of bottom MoO₃ = 70 nm and top MoO₃ = 35 nm. However, we need to limit the thickness of the bottom MoO₃ layer to 5 nm to ensure the efficient charge transport in the interlayer. Hence, for optimum OPD performance, we decided that the bottom MoO₃ layer should be fixed to 5 nm with 10 nm of Ag interlayer and 35 nm of top MoO₃ layer. The star in Fig. 2b indicates the suggested optimum light absorption point of the OPD structure. This choice is expected to guarantee a high charge transport efficiency and a high absorption of the incident light above 90% in the active layer at the same time [23,29].

Additionally, we investigated the influence of the dielectric layer in the DMD electrode on the light reflection properties by studying an optical admittance of the multilayer system [30,31]. The admittance diagram helps to understand more clearly how the variation of each multilayer results in the minimum reflectance of the DMD structure. Fig. 3 presents the admittance diagrams of the multilayer transparent electrodes of Ag 10 nm/MoO₃ 5 nm/glass and MoO₃ 35 nm/Ag 10 nm/MoO₃ 5 nm/glass substrate at 546 nm wavelength, respectively. The loci for perfect electric conductors and optically transparent dielectric materials are represented by a series of circular arcs while the semiconductors result in a spiral locus. As the thickness of each medium increases, the optical admittance of the layer is computed that leads to a rotation of the admittance on either circles or spirals and the

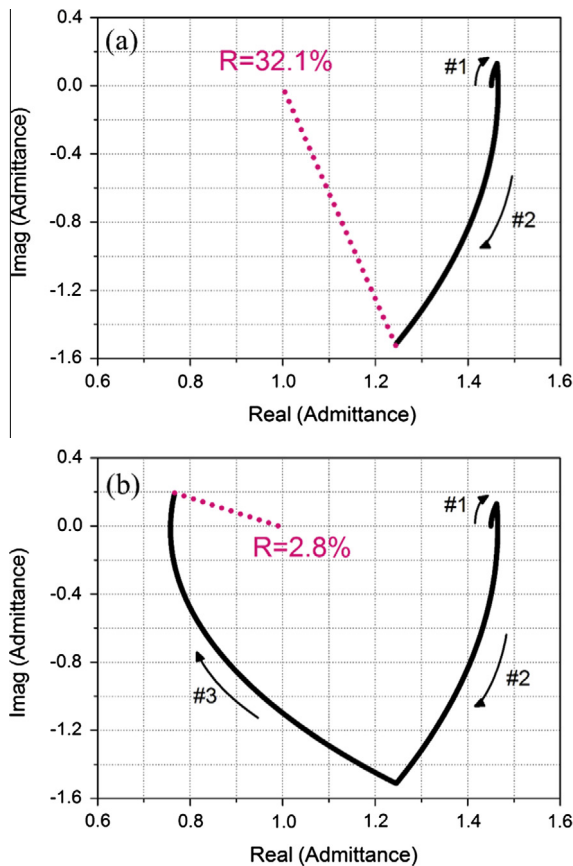


Fig. 3. Admittance diagrams of (a) MoO₃ (5 nm, #1)/Ag (10 nm, #2) DM and (b) MoO₃ (5 nm, #1)/Ag (10 nm, #2)/MoO₃ (35 nm, #3) DMD multilayers on glass substrates. The arrows indicate the increasing thickness of each layer from the glass substrates.

corresponding locus is plotted on the complex plane. The starting point of the admittance diagram is (1.45,0) that corresponds to a glass substrate and the subsequent admittance is determined by both the refractive index and thickness of the material. For example, in Fig. 3a, 5 nm of MoO₃ (#1) leads to the admittance rotating from (1.45,0) toward (1.463,0.131). After that, 10 nm of Ag (#2) results in the rotation of admittance to (1.245, -1.511). When the termination point of the whole multilayer system ends at (1,0) that corresponds to air, a perfect impedance matching occurs, thus giving rise to zero reflection. This implies that reducing the difference between the final admittance point and the air enables the transmission efficiency of the DMD electrode to be enhanced by suppressing the light reflections. For the structure without the top MoO₃ film, the termination point is (1.245, -1.511) that is not close to the air, resulting in 32.1% reflections (*R*), which can be calculated by the following expression.

$$R = \left(\frac{Y_0 - Y_1}{Y_0 + Y_1} \right) \left(\frac{Y_0 - Y_1}{Y_0 + Y_1} \right)^* \quad (1)$$

where Y_0 and Y_1 are the optical admittance of the incident medium (i.e. air) and the termination point, respectively [31].

In contrast, in Fig. 3b, the admittance obtained from the multilayer structure with the top MoO₃ layer (#3) ends at (0.766,0.183), which is much close to the point of the air, thereby leading to highly suppressed reflections of 2.8%. Such highly reduced reflections can also be explained by a small index difference between air and MoO₃ as compared to a large difference between air and metallic layer.

Fig. 4 shows excellent agreement between simulated data obtained by the transfer matrix method and the experimental optical transmission and reflectance spectra of the both MoO₃ 5 nm/Ag 10 nm/MoO₃ 35 nm DMD and MoO₃ 5 nm/Ag 10 nm DM electrodes on glass substrates at normal incidence. It is noticed that the maximum light transmittance of 85.7% is achieved at 468 nm wavelength for the DMD electrode on glass. We also note that the light transmittance of the optimized DMD electrode is comparable with that of a standard ITO glass (Delta technologies, $R_{\text{sheet}} \sim 11 \Omega/\text{sq}$), as included in Fig. 4. The transmittance of the DMD electrode at 546 nm wavelength was 76.8%, which is much higher than that of DM electrode of 56% at same wavelength. On the other hands, the measured reflectance of the DMD multilayer at 546 nm wavelength was 5.4% while the DM structure showed 37.6% of the reflectance. These measured reflectance values are in good agreement with the calculated reflectance values from both the simulated reflectance spectrum in Fig. 4 and the admittance diagram in Fig. 3.

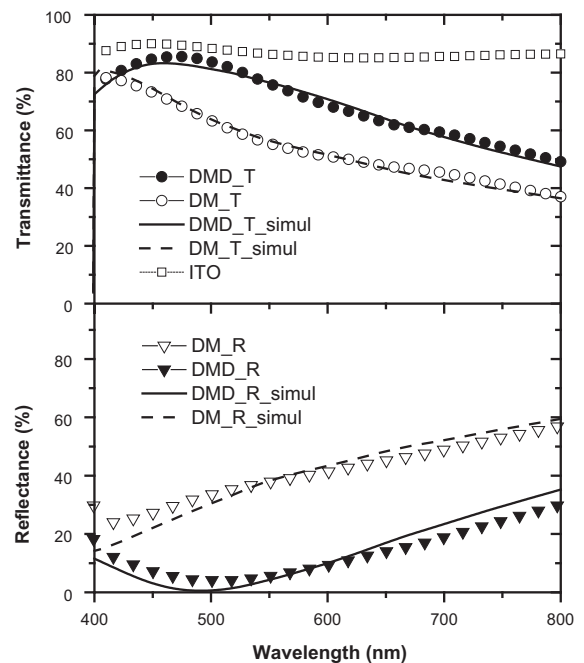


Fig. 4. Experimental and simulated optical transmittance and reflectance spectra of the optimal DMD (MoO₃ 5 nm/Ag 10 nm/MoO₃ 35 nm) and DM (MoO₃ 5 nm/Ag 10 nm) multilayer. Transmission spectra (top) shows excellent match with experimental spectra (DMD: closed circle, DM: open circle) with simulation plot (DMD: solid line, DM: dashed line). Transmission spectrum of ITO film (open square) is included for comparison. Reflectance spectra (bottom) is shown with experimental spectra (DMD: closed triangle, DM: open triangle) with simulation plot (DMD: solid line, DM: dashed line) in good agreement.

3.2. Device physics of the top illuminated anode DMD OPD

The top illuminated anode OPD incorporates several functional layers including cathode (Al), electron transfer layer (ETL, ZnO), bulk heterojunction (BHJ, P3HT:PCBM) photoactive layer, hole transfer layer (HTL, bottom MoO₃), anode (Ag), and anti-reflection layer (top MoO₃). Fig. 5a shows band diagram of the OPD with corresponding energy levels for each layer. The superpositioned layers in BHJ region with solid line and dashed line represent energy band of P3HT electron donor and PCBM electron acceptor, respectively. Note that the good alignment of the conduction band of the ZnO layer (4.4 eV [32]) with the lowest unoccupied molecular orbital (LUMO) level of PCBM (4.3 eV [33]) and the conduction band of the MoO₃ layer (5.5 eV [34]) with the highest occupied molecular orbital (HOMO) level of P3HT (5.0 eV [33]) forms favorable energy level match between buffer layers and BHJ active layer.

Under equilibrium condition, we assume that MoO₃ layer forms ohmic contact with Ag anode [29], while Al cathode is Fermi-level pinned to ZnO layer forming Schottky junction. The device band bending under equilibrium condition is depicted in Fig. 5b. Although both ZnO and MoO₃ buffer layers employed in the OPD structure are n-type semiconductor [16,34], the high workfunction difference between ZnO ($\Phi_{\text{ZnO}} = 4.7 \text{ eV}$ [32]) and MoO₃ ($\Phi_{\text{MoO}_3} = 5.7 \text{ eV}$ [34]) makes electrons on ZnO cathode side migrate to MoO₃ anode side, establishing the internal electric field inside the BHJ active layer as shown in the figure. Under light illumination condition, the internal E-field allows photo-generated electrons and holes in the active layer drift to the ZnO cathode and MoO₃ anode, respectively, which is the generation principle of the short circuit current when the OPD works in photovoltaic regime with zero bias.

When the OPD is reverse biased, (positive bias to Al/ZnO cathode and negative bias to MoO₃/Ag) in dark condition, as shown in Fig. 5c, the reverse dark saturation current is mainly generated by undesired charge injection through electrodes, which can be minimized by formation of energetic barriers on each electrode by ZnO and MoO₃ layer [35]. To decrease the dark current at cathode side, the ZnO layer is employed as a hole blocking layer (HBL) to increase the injection barrier for holes to BHJ active layer as $\Delta E_{\text{cathode}} = \text{valence band of ZnO (7.7 eV [16])} - \Phi_{\text{Al}} (4.2 \text{ eV}) = 3.5 \text{ eV}$. On the other hand, the energetic barrier for carrier injection on anode side is $\Delta E_{\text{anode}} = \Phi_{\text{MoO}_3} (5.7 \text{ eV}) - \text{LUMO}_{\text{PCBM}} (4.3 \text{ eV}) = 1.4 \text{ eV}$, which has lower barrier than cathode side. Due to its lower energetic barrier formed on active layer/MoO₃ interface, the dominant electron injection will occur at the anode side.

Under light illumination, (i) excitons are generated by photon absorption in P3HT electron donor, and (ii) excitons diffuse to the electron acceptor–donor interface. (iii) The diffused excitons dissociate into electron–hole pairs due to internal electric field. (iv) Finally, the electrons and holes transport by hopping between localized states and collected by cathode and anode, respectively, generating photocurrent in the OPD [36].

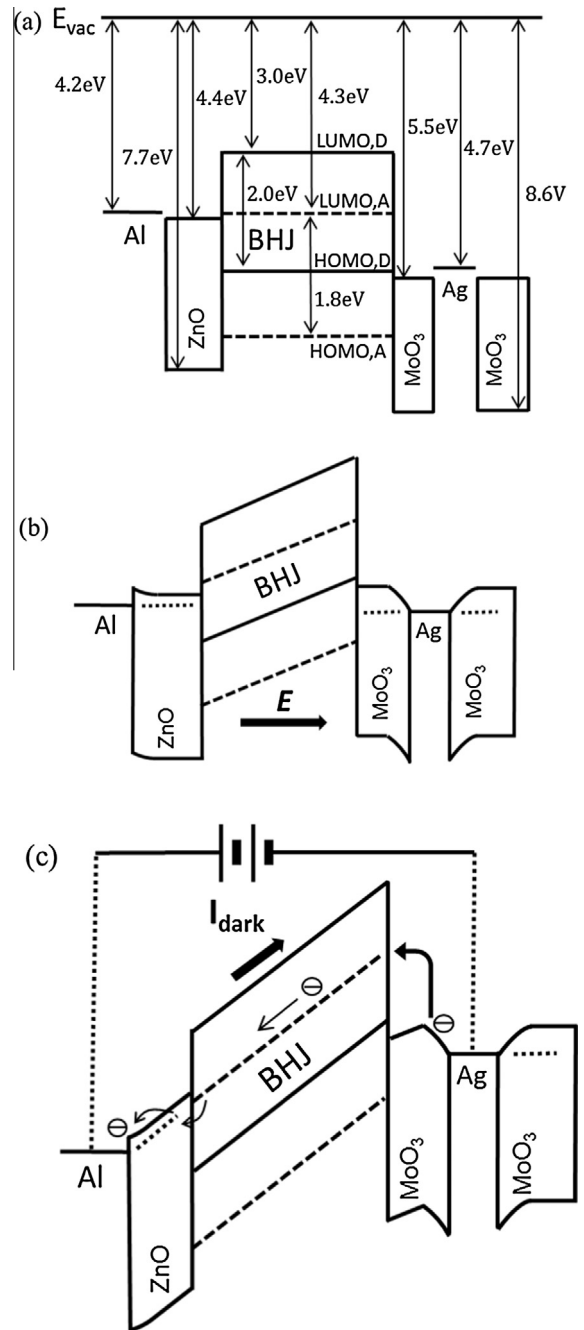


Fig. 5. (a) Band energy diagram of the P3HT:PCBM OPD under open circuit condition. D indicates the P3HT electron donor while A is PCBM electron acceptor. (b) Schematic band diagram of the top anode OPD in equilibrium under dark condition. (c) Band diagram of the OPD with reverse bias under dark condition. The arrows show the carrier injection mechanism at each electrode and the direction of dark current.

3.3. Electrical characteristics of the top anode DMD OPDs

To validate the suitability of the P3HT:PCBM BHJ layer for the indirect type imager with CsI(Tl) scintillator, absorption coefficient of the fabricated P3HT:PCBM film

is compared with the emission spectra of CsI(Tl) scintillator in Fig. 6a. The absorption coefficient α was derived from the measured absorption spectrum of the P3HT:PCBM layer with thickness of 200 nm deposited on glass. The emission spectrum of CsI(Tl) scintillator shown in Fig. 6a is adapted from [37]. As shown in the figure, the absorption coefficient of the P3HT:PCBM film overlaps well with the emission spectrum of the CsI(Tl) scintillator.

To optimize device performance, the top anode OPDs with the active layer of 200 nm, 320 nm and 450 nm were fabricated and investigated. Fig. 6b shows the current density (J) versus voltage (V) characteristics of the top anode OPDs with different active layer thicknesses. The figure confirms that the dark current value of the OPDs increases with decreasing active layer thickness and increasing reverse bias voltage. The trends indicate that the carrier injection occurs from device contacts to photoactive layer and the injection mechanism is attributed to electric-field assisted electron injection from the MoO₃/Ag contact to the LUMO level of PCBM where the lowest energetic barrier exists [35,38]. To validate the E-field driven injection mechanism, the dark current densities are plotted as a function of the internal E-field in Fig. 6c with a relationship $E = V/d$, where E is the internal E-field, V is applied reverse

bias and d is thickness of each active layer. In the figure, note that the $J_{\text{dark}} = 2.22 \times 10^{-7} \text{ A/cm}^2$ of 320 nm active layer device is almost identical with $J_{\text{dark}} = 2.49 \times 10^{-7} \text{ A/cm}^2$ of 450 nm device at $E = 3 \times 10^6 \text{ V/m}$ with negligible error. It is worthwhile to emphasize that the J_{dark} of 320 nm device is even smaller than J_{dark} of 450 nm device at $E = 3 \times 10^6 \text{ V/m}$ compared to the trend of higher J_{dark} of 320 nm device than J_{dark} of 450 nm device in Fig. 6b. The larger variation of J_{dark} of 200 nm device in Fig. 6c could originate from imperfect and unfavorable BHJ morphology with pin-holes developed due to thin active layer [35,39]. However, the data is still acceptable since the J_{dark} of 200 nm device is $5.8 \times 10^{-7} \text{ A/cm}^2$ at $E = 3 \times 10^6 \text{ V/m}$, which is only about two times bigger than J_{dark} value of 320 nm and 450 nm devices at same E-field, when the J_{dark} value of 200 nm device at 1.5 V reverse bias is >10 times bigger than J_{dark} of 320 nm and 450 nm device at the same bias.

To probe existence of traps inside active layers in each device, the dark J - V characteristics of the OPDs are fitted using the non-ideal diode equation given by [40],

$$J_d(V) = J_0 \left[\exp \left(\frac{q(V - J_d(V)R_s)}{nkT} \right) - 1 \right] + \frac{V - J_d(V)R_s}{R_{sh}} \quad (2)$$

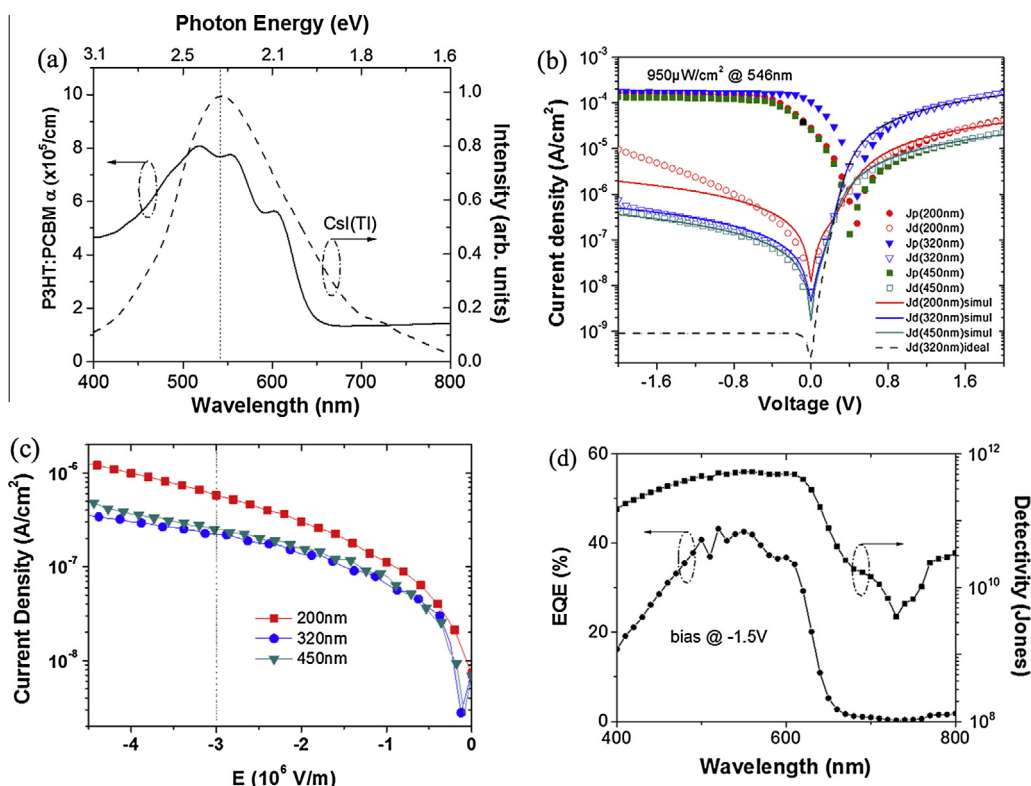


Fig. 6. (a) The absorption coefficient plot of P3HT:PCBM active layer from wavelength 400 nm to 800 nm. (solid line) Emission spectra of CsI(Tl) scintillator is included for comparison. (dashed line) (b) Experimental and fitted current density (J) versus voltage (V) characteristics under dark condition and irradiance of $950 \mu\text{W/cm}^2$ light illumination with 546 nm wavelength of the OPDs with different thickness of the photoactive layer. Open symbols represent measured dark currents when solid symbols are photo responses. The solid lines are fitted dark current densities from non-ideal diode equation. The dashed line represents ideal J - V curve when the shunt resistance R_{sh} is infinite. (c) Dark current density (J_{dark}) measurement plot as function of the internal electric field for the OPDs with different active layer thickness. (d) External Quantum Efficiency (EQE) of the OPD with 320 nm thickness active layer at reverse bias of 1.5 V. The right axis indicates specific detectivity of the OPD according to wavelength from 400 nm to 800 nm.

where J_d is total dark current density, J_0 is reverse dark saturation current density, n is ideality factor, k is Boltzmann constant, T is temperature, R_s is series resistance, and R_{sh} is shunt resistance. The fitted curves are included in Fig. 6b showing a very good agreement to experimental data. The fitting of Eq. (2) to the dark J - V characteristics yielded $n = 1.95$, $R_{sh} = 1 \text{ M}\Omega \text{ cm}^2$ for 200 nm device, $n = 1.6$, $R_{sh} = 4 \text{ M}\Omega \text{ cm}^2$ for 320 nm device, $n = 1.5$, $R_{sh} = 5.5 \text{ M}\Omega \text{ cm}^2$ for 450 nm device, respectively. The ideality factor deviation from unity can be associated with deep trapped carrier or trap-assisted recombination mechanism [41,42]. The larger ideality factor values observed for thinner active layer devices can be explained by larger density of pin-holes and defects present in thinner active films; they can be responsible for larger trap-assisted recombination. The increasing shunt resistance values from 1 M Ω to 5.5 M Ω for thicker active layer supports decrease of the current leakage with increase of film thickness. From the fitted parameters and Eq. (2), we can estimate the theoretical limit of the total dark current density $J_{d,\min}$ of fabricated OPD by setting the shunt resistance R_{sh} value to infinite, i.e. there is no shunt leakage through the device. The dashed line in Fig. 6b represents the ideal J - V curve of the OPD and the corresponding $J_{d,\min}$ value converges to $9 \times 10^{-10} \text{ A/cm}^2$, which is identical to the value of reverse dark saturation current density J_0 .

It is worthwhile to point out that the dark current values were measured for OPDs with bar-type electrodes. Because of the difficulty in making electrical contact for top-illumination type OPDs with DMD top electrode, we utilized vertically aligned bar-shape pattern to ensure the extraction of cathode/anode contacts. The structure is inherently prone to have higher leakage current through the edge of the patterned electrodes on bottom side due to significant height difference between Al cathode (100 nm) and spin-coated ZnO buffer layer (40 nm). To verify this statement, we fabricated an OPD with non-patterned ITO/ZnO cathode and island-type top anode (MoO₃ 5 nm/Ag 100 nm) for bottom illumination geometry, while the process of other layers was kept same. By adapting the non-patterned ITO cathode as bottom electrode, we can exclude the leakage current through the edge of the electrode. The measured dark current value from such device was $6.6 \times 10^{-9} \text{ A/cm}^2$ at 1.5 V reverse bias. This value is two order smaller than the dark current value of the bar-type OPD and even approaches the estimated theoretical limit of the dark current density, $J_{d,\min}$. The details of device structure and corresponding J - V curve can be found in Fig. S2 from Supplementary Materials. These results indicate that the dark leakage current can be different for top-illuminated OPD from that for bottom-illuminated

OPD. Hence top-illuminated anode OPD should be able to achieve low dark current once device structure is optimized.

Table 1 summarized the top anode OPDs' figures of merit including J_{dark} , Responsivity (\mathcal{R}), External Quantum Efficiency (EQE), Noise Equivalent Power (NEP), and Specific Detectivity (D^*). \mathcal{R} and EQE are calculated by Eq. (S1) and NEP and D^* are derived from Eqs. (S2-2) and (S3), respectively. [See Supplementary Materials for detailed description of each figure of merit.] In the table, even though the dark current of OPD with 450 nm active layer thickness showed lowest value of $2.95 \times 10^{-7} \text{ A/cm}^2$ compared to $3.81 \times 10^{-7} \text{ A/cm}^2$ of OPD with 320 nm active layer and $4.25 \times 10^{-6} \text{ A/cm}^2$ of OPD with 200 nm active layer at reverse bias of 1.5 V, higher responsivity of 320 nm OPD (0.18 A/W) than 450 nm OPD (0.14 A/W) yielded the highest specific detectivity of 5.25×10^{11} Jones among all the devices. This value is comparable to the value ($D^* = 8.8 \times 10^{11}$ Jones) reported by Tedde et al. in their bottom-illuminated spray coated OPDs [43] and even higher than the detectivity value of 3.15×10^{11} Jones reported by Arredondo et al. for their ITO-free inverted P3HT:PCBM photodetectors [44]. Fig. 6d shows the measured EQE of the OPD with 320 nm active layer along with specific detectivity D^* plotted versus wavelength in logarithmic scale. The EQE and D^* were measured under reverse bias 1.5 V. The peak EQE value of 42.6% at 546 nm wavelength in the figure shows a good agreement with the calculated value in Table 1. Fig. 7a shows the J - V characteristics of top anode OPD with 320 nm active layer for various light intensities of the 546 nm wavelength illumination. The graph clearly shows that the top anode OPD can response to light irradiance from $950 \mu\text{W/cm}^2$ down to 780 nW/cm^2 . While the photocurrent at the negative bias increases with higher light intensity, the photocurrent at positive bias 1 V has no variation, indicating the series resistance R_s of the top anode OPD is not affected by the irradiance. Fig. 7b shows fitted linear dynamic range (LDR) of the photocurrent according to input irradiance in Fig. 7a at reverse bias of 1.5 V. The lower limit of the range was defined by the dark current value of the OPD, which is $3.8 \times 10^{-7} \text{ A/cm}^2$ for the OPD with 320 nm active layer. The photocurrent is found to increase linearly with irradiance of 546 nm wavelength up to 1 mW/cm^2 . The LDR graph can be described by a linear equation, $J \text{ (A/cm}^2\text{)} = \alpha P_{\text{in}} \text{ (}\mu\text{W/cm}^2\text{)} + \beta$ with coefficients $\alpha = 0.108 \text{ (A/W)}$ and $\beta = -1.51 \times 10^{-6} \text{ (A/cm}^2\text{)}$, where J is the photocurrent and P_{in} is input irradiance. Note that the minimum J value in the equation is limited by the dark current value of the top anode OPD. The calculated LDR of the OPD from Eq. (S4) was 60 dB, comparable to

Table 1

Comparison of photodiode figures of merit with different thickness of P3HT:PCBM active layer of 200 nm, 320 nm and 450 nm.

P3HT:PCBM thickness (nm)	J_{dark} @ -1.5 V (A/cm ²)	Responsivity @ -1.5 V (A/W)	EQE @ -1.5 V (%)	NEP (W/Hz ^{1/2})	D^* (Jones)
200	4.25×10^{-6}	0.17	38	1.37×10^{-12}	1.46×10^{11}
320	3.81×10^{-7}	0.18	42	3.81×10^{-13}	5.25×10^{11}
450	2.95×10^{-7}	0.14	31	4.46×10^{-13}	4.49×10^{11}

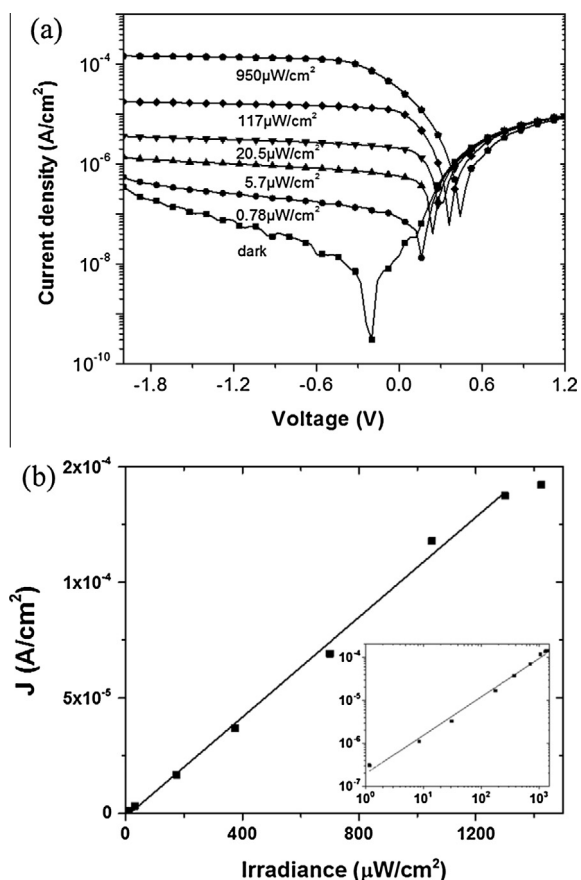


Fig. 7. (a) J - V curve of the top anode OPD with 320 nm active layer thickness under various light intensity at 546 nm light wavelength. (b) Linear dynamic range (LDR) plot of the OPD with 320 nm active layer thickness measured at reverse bias of 1.5 V. The photocurrent density J is the summation of dark current and photo-generated current, $J = J_{\text{dark}} + J_{\text{ph}}$ when the irradiance is 546 nm wavelength monochromatic illumination. The inset is the LDR plot in logarithmic scale.

the LDR of InGaAs photodetectors [45], which is sufficient for a high contrast imaging.

4. Conclusion

In conclusion, we suggested the top anode OPD with $\text{MoO}_3/\text{Ag}/\text{MoO}_3$ semi-transparent electrode for top illumination. The DMD top transparent electrode for the OPD is simulated and optimized to acquire the best light absorption condition for CsI(Tl) scintillator light emission spectrum of 545 nm wavelength. The fabricated DMD transparent electrode showed the maximum optical transmittance of 85.7% with $R_{\text{sheet}} = 6.2 \Omega/\text{sq}$, which is suitable for large area imager application. Moreover, P3HT:PCBM active layer was optimized for the inverted OPD structure to yield the high detectivity of 5.25×10^{11} Jones. The OPD with inverted structure will enhance the stability of the OPD significantly when the top incoupling MoO_3 layer allows direct deposition of scintillator material over OPD. The OPDs with such structure are ready-to-be integrated on various applications especially to cost-effective large area X-ray imager.

Acknowledgements

The authors would like to thank Byeongseop Song for DMD anode deposition and Kyusang Lee for EQE measurement. H.K. is recipient of the Korea Foundation for Advanced Studies (KFAS) fellowship. C.M.Z. is recipient of EECs department fellowship.

Appendix A. Supplementary material

Supplementary data associated with this article can be found, in the online version, at <http://dx.doi.org/10.1016/j.orgel.2015.02.012>.

References

- [1] L. Dou, J. You, Z. Hong, Z. Xu, G. Li, R.A. Street, et al., 25th Anniversary article : a decade of organic/polymeric photovoltaic research, *Adv. Mater.* 25 (2013) 6642–6671, <http://dx.doi.org/10.1002/adma.201302563>.
- [2] K.-J. Baeg, M. Binda, D. Natali, M. Caironi, Y.-Y. Noh, Organic light detectors: photodiodes and phototransistors, *Adv. Mater.* 25 (2013) 4267–4295, <http://dx.doi.org/10.1002/adma.201204979>.
- [3] T.N. Ng, W.S. Wong, M.L. Chabiny, S. Sambandan, R.A. Street, Flexible image sensor array with bulk heterojunction organic photodiode, *Appl. Phys. Lett.* 92 (2008) 213303, <http://dx.doi.org/10.1063/1.2937018>.
- [4] S. Tedde, E.S. Zaus, J. Fürst, D. Henseler, P. Lugli, Active pixel concept combined with organic photodiode for imaging devices, *IEEE Electron Dev. Lett.* 28 (2007) 893–895.
- [5] G.H. Gelinck, A. Kumar, D. Moet, J. Van Der Steen, U. Shafique, P.E. Malinowski, et al., X-ray imager using solution processed organic transistor arrays and bulk heterojunction photodiodes on thin, flexible plastic substrate, *Org. Electron.* 14 (2013) 2602–2609, <http://dx.doi.org/10.1016/j.orgel.2013.06.020>.
- [6] W. Zhao, G. Ristic, J.A. Rowlands, X-ray imaging performance of structured cesium iodide scintillators, *Med. Phys.* 31 (2004) 2594, <http://dx.doi.org/10.1118/1.1782676>.
- [7] C. Zhao, J. Kanicki, Amorphous In–Ga–Zn–O thin-film transistor active pixel sensor X-ray imager for digital breast tomosynthesis, *Med. Phys.* 41 (2014) 091902, <http://dx.doi.org/10.1118/1.4892382>.
- [8] F. Arca, E. Kohlstädt, S.F. Tedde, P. Lugli, O. Hayden, Large active area organic photodiodes for short-pulse X-ray detection, *IEEE Trans. Electron Dev.* 60 (2013) 1663–1667, <http://dx.doi.org/10.1109/TED.2013.2250974>.
- [9] T. Agostinelli, M. Campoy-Quiles, J.C. Blakesley, R. Speller, D.D.C. Bradley, J. Nelson, A polymer/fullerene based photodetector with extremely low dark current for X-ray medical imaging applications, *Appl. Phys. Lett.* 93 (2008) 203305, <http://dx.doi.org/10.1063/1.3028640>.
- [10] B. Zimmermann, U. Würfel, M. Niggemann, Longterm stability of efficient inverted P3HT:PCBM solar cells, *Sol. Energy Mater. Sol. Cells* 93 (2009) 491–496, <http://dx.doi.org/10.1016/j.solmat.2008.12.022>.
- [11] Z. He, C. Zhong, S. Su, M. Xu, H. Wu, Y. Cao, Enhanced power-conversion efficiency in polymer solar cells using an inverted device structure, *Nat. Photon.* 6 (2012) 593–597, <http://dx.doi.org/10.1038/nphoton.2012.190>.
- [12] S.K. Hau, H.-L. Yip, N.S. Baek, J. Zou, K. O'Malley, A.K.-Y. Jen, Air-stable inverted flexible polymer solar cells using zinc oxide nanoparticles as an electron selective layer, *Appl. Phys. Lett.* 92 (2008) 253301, <http://dx.doi.org/10.1063/1.2945281>.
- [13] A.K.K. Kyaw, X.W. Sun, C.Y. Jiang, G.Q. Lo, D.W. Zhao, D.L. Kwong, An inverted organic solar cell employing a sol-gel derived ZnO electron selective layer and thermal evaporated MoO_3 hole selective layer, *Appl. Phys. Lett.* 93 (2008) 221107, <http://dx.doi.org/10.1063/1.3039076>.
- [14] G. Li, C.-W. Chu, V. Shrotriya, J. Huang, Y. Yang, Efficient inverted polymer solar cells, *Appl. Phys. Lett.* 88 (2006) 253503, <http://dx.doi.org/10.1063/1.2212270>.
- [15] X. Liu, H. Wang, T. Yang, W. Zhang, I.-F. Hsieh, S.Z.D.D. Cheng, et al., Solution-processed near-infrared polymer photodetectors with an inverted device structure, *Org. Electron.* 13 (2012) 2929–2934, <http://dx.doi.org/10.1016/j.orgel.2012.08.017>.

- [16] J. Jeong, S. Nam, H. Kim, Y. Kim, Inverted organic photodetectors with ZnO electron-collecting buffer layers and polymer bulk heterojunction active layers, *IEEE J. Sel. Top. Quantum Electron.* (2014), <http://dx.doi.org/10.1109/JSTQE.2014.2354649>, 1–1.
- [17] D. Baierl, B. Fabel, P. Gabos, L. Pancheri, P. Lugli, G. Scarpa, Solution-processable inverted organic photodetectors using oxygen plasma treatment, *Org. Electron.* 11 (2010) 1199–1206, <http://dx.doi.org/10.1016/j.orgel.2010.04.023>.
- [18] D. Baierl, B. Fabel, P. Lugli, G. Scarpa, Efficient indium-tin-oxide (ITO) free top-absorbing organic photodetector with highly transparent polymer top electrode, *Org. Electron.* 12 (2011) 1669–1673, <http://dx.doi.org/10.1016/j.orgel.2011.06.021>.
- [19] M. Jørgensen, K. Norrman, F.C. Krebs, Stability/degradation of polymer solar cells, *Sol. Energy Mater. Sol. Cells* 92 (2008) 686–714, <http://dx.doi.org/10.1016/j.solmat.2008.01.005>.
- [20] C. Zhang, D. Zhao, D. Gu, H. Kim, T. Ling, Y.R. Wu, et al., An ultrathin, smooth, and low-loss Al-doped Ag film and its application as a transparent electrode in organic photovoltaics, *Adv. Mater.* 26 (2014) 5696–5701, <http://dx.doi.org/10.1002/adma.201306091>.
- [21] C.-C. Chueh, S.-C. Chien, H.-L. Yip, J.F. Salinas, C.-Z. Li, K.-S. Chen, et al., Toward high-performance semi-transparent polymer solar cells: optimization of ultra-thin light absorbing layer and transparent cathode architecture, *Adv. Energy Mater.* 3 (2013) 417–423, <http://dx.doi.org/10.1002/aenm.201200679>.
- [22] K. Hong, K. Kim, S. Kim, I. Lee, H. Cho, S. Yoo, et al., Optical properties of WO₃/Ag/WO₃ multilayer as transparent cathode in top-emitting organic light emitting diodes, *J. Phys. Chem. C* 115 (2011) 3453–3459.
- [23] B. Tian, G. Williams, D. Ban, H. Aziz, Transparent organic light-emitting devices using a MoO₃/Ag/MoO₃ cathode, *J. Appl. Phys.* 110 (2011) 104507, <http://dx.doi.org/10.1063/1.3662194>.
- [24] T. Winkler, H. Schmidt, H. Flügge, F. Nikolayzik, I. Baumann, S. Schmale, et al., Efficient large area semitransparent organic solar cells based on highly transparent and conductive ZTO/Ag/ZTO multilayer top electrodes, *Org. Electron.* 12 (2011) 1612–1618, <http://dx.doi.org/10.1016/j.orgel.2011.06.015>.
- [25] J.Y. Lee, K.-T. Lee, S. Seo, L.J. Guo, Decorative power generating panels creating angle insensitive transmissive colors, *Sci. Rep.* 4 (2014) 4192, <http://dx.doi.org/10.1038/srep04192>.
- [26] K. Lee, J.Y. Lee, S. Seo, L.J. Guo, Colored ultrathin hybrid photovoltaics with high quantum efficiency, *Light Sci. Appl.* 3 (2014) e215, <http://dx.doi.org/10.1038/lsa.2014.96>.
- [27] G. Li, V. Shrotriya, J. Huang, Y. Yao, T. Moriarty, K. Emery, et al., High-efficiency solution processable polymer photovoltaic cells by self-organization of polymer blends, *Nat. Mater.* 4 (2005) 864–868, <http://dx.doi.org/10.1038/nmat1500>.
- [28] D. Yao, M. Gu, X. Liu, S. Huang, B. Liu, C. Ni, Fabrication and performance of columnar CsI(Tl) scintillation films with single preferred orientation, *IEEE Trans. Nucl. Sci.* 60 (2013) 1632–1636.
- [29] D. Nguyen, S. Vedraïne, L. Cattin, P. Torchio, M. Morsli, F. Flory, et al., Effect of the thickness of the MoO₃ layers on optical properties of MoO₃/Ag/MoO₃ multilayer structures, *J. Appl. Phys.* 112 (2012) 063505, <http://dx.doi.org/10.1063/1.4751334>.
- [30] C.C. Lee, S.H. Chen, C.C. Jaing, Optical monitoring of silver-based transparent heat mirrors, *Appl. Opt.* 35 (1996) 5698–5703.
- [31] K.-T. Lee, S. Seo, J.Y. Lee, L.J. Guo, Ultrathin metal-semiconductor-metal resonator for angle invariant visible band transmission filters, *Appl. Phys. Lett.* 104 (2014) 231112, <http://dx.doi.org/10.1063/1.4883494>.
- [32] A. Janotti, C.G. Van de Walle, Fundamentals of zinc oxide as a semiconductor, *Reports Prog. Phys.* 72 (2009) 126501, <http://dx.doi.org/10.1088/0034-4885/72/12/126501>.
- [33] I. Hwang, D. Moses, A.J. Heeger, Photoinduced carrier generation in P3HT/PCBM bulk heterojunction materials, *J. Phys. Chem. C* 112 (2008) 4350–4354.
- [34] A. Kahn, J. Meyer, Electronic structure of molybdenum-oxide films and associated charge injection mechanisms in organic devices, *J. Photon. Energy* 1 (2011) 011109, <http://dx.doi.org/10.1117/1.3555081>.
- [35] P.E. Keivanidis, P.K.H. Ho, R.H. Friend, N.C. Greenham, The dependence of device dark current on the active-layer morphology of solution-processed organic photodetectors, *Adv. Funct. Mater.* 20 (2010) 3895–3903, <http://dx.doi.org/10.1002/adfm.201000967>.
- [36] C. Deibel, V. Dyakonov, Polymer–fullerene bulk heterojunction solar cells, *Reports Prog. Phys.* 73 (2010) 096401, <http://dx.doi.org/10.1088/0034-4885/73/9/096401>.
- [37] B.C. Grabmaier, Crystal scintillators, *IEEE Trans. Nucl. Sci.* NS-31 (1984) 372–376.
- [38] P.E. Keivanidis, S.-H. Khong, P.K.H. Ho, N.C. Greenham, R.H. Friend, All-solution based device engineering of multilayer polymeric photodiodes: minimizing dark current, *Appl. Phys. Lett.* 94 (2009) 173303, <http://dx.doi.org/10.1063/1.3120547>.
- [39] V.D. Mihailetschi, P.W.M. Blom, J.C. Hummelen, M.T. Rispens, Cathode dependence of the open-circuit voltage of polymer:fullerene bulk heterojunction solar cells, *J. Appl. Phys.* 94 (2003) 6849, <http://dx.doi.org/10.1063/1.1620683>.
- [40] C. Waldauf, M.C. Scharber, P. Schilinsky, J.A. Hauch, C.J. Brabec, Physics of organic bulk heterojunction devices for photovoltaic applications, *J. Appl. Phys.* 99 (2006) 104503, <http://dx.doi.org/10.1063/1.2198930>.
- [41] G.A.H. Wetzelaer, M. Kuik, M. Lenes, P.W.M. Blom, Origin of the dark-current ideality factor in polymer:fullerene bulk heterojunction solar cells, *Appl. Phys. Lett.* 99 (2011) 153506, <http://dx.doi.org/10.1063/1.3651752>.
- [42] R.A. Street, M. Schoendorf, A. Roy, J.H. Lee, Interface state recombination in organic solar cells, *Phys. Rev. B* 81 (2010) 205307, <http://dx.doi.org/10.1103/PhysRevB.81.205307>.
- [43] S.F. Tedde, J. Kern, T. Sterzl, J. Fu, P. Lugli, O. Hayden, Fully spray coated organic photodiodes, *Nano Lett.* 9 (2009) 980–983.
- [44] B. Arredondo, C. De Dios, R. Vergaz, a.R.R. Criado, B. Romero, B. Zimmermann, et al., Performance of ITO-free inverted organic bulk heterojunction photodetectors: comparison with standard device architecture, *Org. Electron.* 14 (2013) 2484–2490, <http://dx.doi.org/10.1016/j.orgel.2013.06.018>.
- [45] X. Gong, M. Tong, Y. Xia, W. Cai, J.S. Moon, Y. Cao, et al., High-detectivity polymer photodetectors with spectral response from 300 nm to 1450 nm, *Science* 325 (2009) 1665–1667, <http://dx.doi.org/10.1126/science.1176706>.